Enhancement of Ferromagnetism in Nonmagnetic Metal Oxide Nanoparticles by Facet Engineering

Liyuan Long, Shijie Xiong, Ming Meng, Lizhe Liu, Jinlei Zhang, Xinglong Wu, and Paul K. Chu**

Ferromagnetism in semiconducting metal oxide nanoparticles has been intensively investigated due to their potential applications in spintronics, information storage, and biomedicine. Ferromagnetism can be produced in nonmagnetic metal oxide nanoparticles by a variety of methods or factors, but the saturated magnetization is typically of the order of 10^{-4} emu g^{-1} and too small to be useful in practice. In this work, it is demonstrated theoretically and experimentally that stronger ferromagnetism can be achieved in undoped nonmagnetic metal oxide semiconductors by exposing some specific polar crystal facets with carvings of special bonds via the interaction with underlying vacancies. In_2O_3 microcubes with completely enclosed {001} polar facets show two orders of magnitude enhancement at room temperature compared to nanoparticles with an irregular morphology. The surface magnetic domains on the {001} facets account for the significantly enhanced ferromagnetism. The technique and concept described here can be extended to other types of metal oxide nanostructures to spur their application to spintronics.

1. Introduction

In order to exploit the charge and spin characteristics of electrons simultaneously, researchers have studied semiconductors with room temperature ferromagnetism (FM).[1–5] Although oxide diluted magnetic semiconductors (DMSs) such as ZnO,[5–7] TiO_2,[8] and SnO_2[9] doped with transition metal elements are promising candidates to achieve this goal, there is controversy whether the FM is a direct outcome of their intrinsic properties or due to magnetic metal clusters (dopants) in the semiconductors.[8] In addition, transition metal dopants at high concentrations frequently precipitate in second phases, thereby thwarting attempts to enhance the Curie temperature.[10,11] Since HfO_2 thin films have been reported to be ferromagnetic at room temperature without magnetic metal dopants,[12] various undoped metal oxide films with bulk diamagnetism such as TiO_2, ZnO, and In_2O_3 have been investigated as DMSs and reported to have some attractive properties.[2,13–15] However, since metal oxide films are not ideal in spintronics applications because of the substrates and defects at the interface between the films and substrates as the possible FM origin,[2] perfectly pure and

---

Dr. L. Y. Long, Prof. S. J. Xiong, Dr. L. Z. Liu, Dr. J. L. Zhang, Prof. X. L. Wu
Key Laboratory of Modern Acoustics
MOE
Institute of Acoustics and Collaborative Innovation
Center of Advanced Microstructures
National Laboratory of Solid State Microstructures
Nanjing University
Nanjing 210093, China
E-mail: hkxlwu@nju.edu.cn

Dr. M. Meng
School of Physics and Telecommunications
Engineering
Zhoukou Normal University
Zhoukou 466001, P. R. China

Prof. P. K. Chu
Department of Physics and Materials Science
City University of Hong Kong
Tat Chee Avenue, Kowloon, Hong Kong, China
E-mail: appkchu@cityu.edu.hk

DOI: 10.1002/smll.201602951

homogeneous metal oxide nanoparticles (NPs) are considered more viable in the attempt to understand the FM origin with a high Curie temperature ($T_c > 300$ K).

It has been reported that undoped metal oxide NPs exhibit room temperature FM due to surface oxygen vacancies (OVs),[16–18] but the saturated magnetization is too small to be practical in spintronics applications. Hence, it is important to find new approaches to enhance the FM of pure metal oxides. It is generally recognized that the exchange interactions between localized electron spin moments resulting from cation or anion vacancies on the surface of the NPs account for the weak FM[8,17] and the importance of surface defects instead of bulk defects has been illustrated.[6,18–20] According to the "Stoner criterion," FM induced by the exchange of electronic wavefunctions at the Fermi level can be enhanced by regulating the surface structures and vacancy distributions.[21] Consequently, crystal facets with different atomic arrangements may affect the ferromagnetic properties and polar crystal facets on the metal oxide with abundant dangling bonds may contribute to the coupling effects of the localized spin moments on the surface. Enhancement of FM can originate from the interactions between these surface dangling bonds and cation or anion vacancies near the polar facets which are prevalent on real samples. If this assumption can be verified theoretically, FM in metal oxides can be enhanced by precisely controlling the specific polar crystal facets during sample fabrication.

In_2O_3, a wide gap oxide semiconductor with high optical transparency, electric conductivity, and ferromagnetic Curie temperature, is one of the promising oxide DMSs.[15,22–25] It has been shown in our previous experiments that morphologically homogeneous In_2O_3 microcrystals (MCs) enclosed with different crystal facets can be prepared controllably on a large scale.[26,27] Herein, we select In_2O_3 as the model material to investigate the relationship between crystal facets and FM and an enhancement of two orders of magnitude is observed at room temperature compared to NPs with an irregular morphology.

2. Results and Discussion

A first-principle study is first conducted on the electronic structure of the In_2O_3 film with the surface along the {001} direction (note that the {111} and {022} facets are nonpolar[27]). The calculation is performed using the generalized gradient approximation of the Perdew, Burke, and Ernzerhof form[28] under package CASTEP[29] in which a plane-wave norm-conserving pseudopotential method[30] is employed. A kinetic energy cutoff of 500 eV is adopted to represent the single-particle wave functions and the Monkhorst–Pack k-point meshes of $6 \times 6 \times 1$ are used. Slabs are utilized to investigate the band structure and wave functions of the {001} surface of the In_2O_3. To form a periodic lattice, the slabs with a thickness of 1.37 nm are stacked periodically and separated by vacuum slabs with a thickness of 1.17 nm. The supercell along the surface is a square with dimensions of 1.01×1.01 nm^2. The geometry of the configuration is optimized by the Broyden-Fletcher-Goldfarb-Shanno (BFGS) minimizer in the CASTEP package with default convergence tolerances: 2×10^{-5} eV for energy change, 0.5 eV nm^{-1} for maximum force, and 2×10^{-4} nm for maximum displacement,[31] which have been tested to converge. After geometric optimization, the spin-polarized band structure and orbitals of electrons are calculated using the CASTEP package.

To theoretically derive the magnetism, a first-principle study is conducted on the spin-polarized electronic structure of the In_2O_3 film with the polar surface along the {001} direction. **Figure 1** plots the spin-resolved partial density of states (SRPDOS) near the Fermi level and spatial distribution of electron orbitals of relevant states for the {001} slab with two OVs per supercell near the indium-terminated surface. All the states near the Fermi level correspond to the orbitals at and near the oxygen-terminated surface. They are spin-polarized and partially occupied (below the Fermi level) and the occupied states have a net magnetic moment. The spatial distribution of spin is shown in Figure S1 of the Supporting Information. We suggest that Stoner magnetization of the surface states due to the Coulomb interaction of surface itinerant electrons is responsible for the magnetism calculated below.

The electronic spin of cations in insulating oxides is normally coupled with the nearest-neighbor interactions – either superexchange or double exchange.[32] However, this is not the case here because both In and O are not magnetic. The magnetic moments are produced by the spin unbalance in the itinerant electrons in surface states via the electron–electron repulsion interaction. This surface band structure can be described by the Hubbard model

$$H = t \sum_{\langle i,j\rangle,\sigma} c^{\dagger}_{i,\sigma} c_{j,\sigma} + \varepsilon_0 \sum_{i,\sigma} c^{\dagger}_{i,\sigma} c_{i,\sigma} + U \sum_{i} c^{\dagger}_{i,\uparrow} c_{i,\uparrow} c^{\dagger}_{i,\downarrow} c_{i,\downarrow} \tag{1}$$

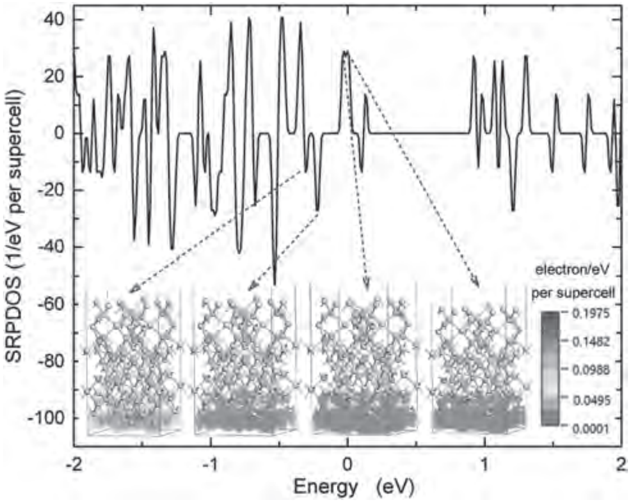

Figure 1. Spin-resolved partial density of states (SRPDOS) of an In_2O_3 slab in the {001} direction with two OVs per supercell near the indium-terminated surface and the orbitals of states near the Fermi level. The lower panel shows the spatial distribution of states near the Fermi level. All the states near the Fermi level are on the O-terminated surface and the spin-up and spin-down subbands are separated. The fillings of spin-up and spin-down subbands are different.

where $c_{i,}\sigma$ ($c_{i,\sigma}^{\dagger}$) is the annihilation (creation) operator of the electron at site i and with spin σ, t is the nearest-neighbor hopping integral, ε_0 is the central energy level of itinerant electrons measured from the Fermi level, and U is the on-site Coulomb interaction. In the present case, t is determined by the width of the spin subband W, namely, $t \approx W/8$, while ε_0 and U depend on the energy of the two spin subbands and occupation of electrons in them. If the occupation per site is x ($2 \geq x \geq 0$), then $U \approx \begin{cases} D/x, 1 > x > 0; \\ D/(2-x), 2 > x > 1, \end{cases}$ with D being the energy difference between two spin subbands, and the saturate magnetization per site is $M_0 \approx \begin{cases} x\mu_{\mathrm{B}}, 1 > x > 0; \\ (2-x)\mu_{\mathrm{B}}, 2 > x > 1, \end{cases}$ with μ_{B} being the Bohr magneton. According to the first-principle derivation, $x \approx 1.7$ for the case without OVs and indium vacancies (IVs) (Figure S1a, Supporting Information), $\varepsilon_0 \approx 0.26$ eV, and $U \approx 0.8$ eV >> t. Introducing OVs (IVs) will increase (decrease) the occupation x. Because the magnetism reaches the maximum at $x = 1$ while vanishing at $x = 0$ and 2, introducing OVs is easier to quench the surface magnetism than introducing IVs as originally $x \approx 1.7$ is closer to 2, as shown in Figure S1b–d of the Supporting Information. Hence, the maximum magnetism is obtained by adjusting the densities of OVs and IVs near the surface. Furthermore, as long as the surface magnetism is not quenched by vacancies, Stoner magnetism can be extended to the states near the vacancies, as shown in Figure S1d of the Supporting Information. Consequently, introducing vacancies near the surface can introduce surface magnetism which appears much thicker than that rendered by only one atomic layer. This is crucial for MCs with a micrometer size. With regard to Stoner FM, the Curie temperature depends on U and x, and from the value of U (0.8 eV), the room temperature FM can be easily obtained if x is adjusted to be close to 1. We also calculate the spatial distributions of magnetic moments of an In_2O_3 slab in the {111} direction and present the typical results with two OVs in Figure S2 of the Supporting Information. It can be seen that the {111} surface shows negligible magnetism.

To experimentally verify the crystal facet- and vacancy-dependent magnetism, four kinds of homogeneous In_2O_3 MCs with different morphologies as shown in **Figure 2** are prepared.[26,27] They are crystalline with a uniform size of about 1 µm and enclosed with no more than two crystal facets of {001} and {111}. Figure 2a depicts the cubic In_2O_3 MCs enclosed with six high-energy {001} facets and the inset shows a simulated cube together with the percentage defined as the area ratio of the {001} facets to total facets. Figure 2b,c shows the cuboctahedral and truncated octahedral In_2O_3 MCs with smaller percentages of the exposed {001} facets and Figure 2d displays the In_2O_3 MCs with the perfect octahedron morphology fully enclosed by low-energy {111} facets. Obviously, the percentages of the exposed {001} facets decrease from 100% to nearly 0% among the four In_2O_3 MCs. The size distributions of the four kinds of MC particles are presented in Figure S3 (Supporting Information) which shows that each of the In_2O_3 MC samples possesses a uniform particle size (slightly more than 1 µm). The powder X-ray diffraction (XRD) patterns published in our previous paper[26] confirm that the four samples have the bcc structure of In_2O_3. For comparison, In_2O_3 NPs with an irregular morphology and no specific exposed crystal facets are also prepared. The scanning electron microscopy (SEM) image and XRD pattern are presented in Figure S4 of the Supporting Information. All the diffraction peaks can be indexed to the bcc structure of In_2O_3 (JCPDS card No. 06-416) and there is no preferred orientation growth. According to the size distribution of the irregular In_2O_3 NPs (Figure S5, Supporting Information), the size of these NPs ranges between 50 and 200 nm.

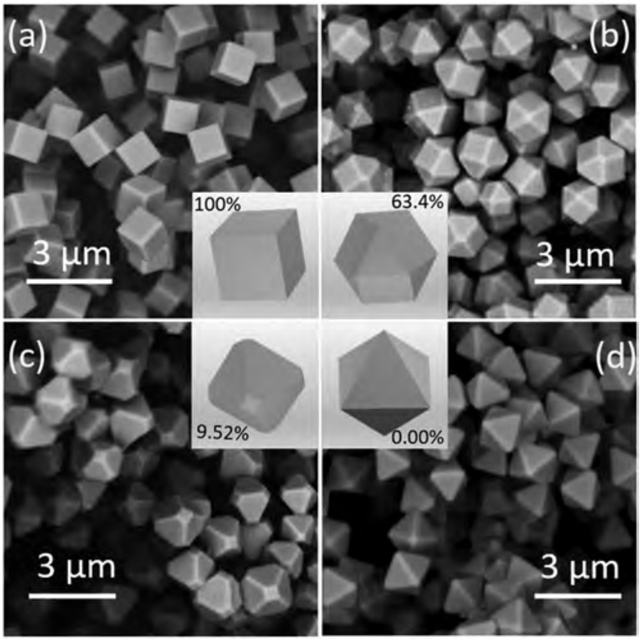

Figure 2. SEM images and simulated diagrams of four In_2O_3 MC samples with different morphologies: a) cube, b) cuboctahedron, c) truncated octahedron, and d) octahedron. The percentages shown in the four simulated images are the area ratios of the exposed {001} facets to total exposed facets.

The room temperature magnetic properties of the four In_2O_3 MC samples are presented in **Figure 3**. They all show obvious ferromagnetic hysteresis with nonzero residual magnetization and coercivity after subtracting the diamagnetic background, implying that these In_2O_3 MCs exhibit room temperature FM. The saturated magnetization of the cubic In_2O_3 MCs (4.4×10^{-2} emu g^{-1}) is ten times larger than that of the octahedron In_2O_3 MCs (2.7×10^{-3} emu g^{-1}). Moreover, the cuboctahedral In_2O_3 MCs exhibit stronger FM than the truncated octahedral and both of them possess saturated magnetization smaller than that of the cubic In_2O_3 but larger than that of the octahedral In_2O_3. This indicates that the saturated magnetization of In_2O_3 MCs is positively related to the percentage of the exposed {001} facets. Here, it is noted that a hysteresis loop is still observed from the octahedron sample because a few truncated octahedrons inevitably exist in the octahedron powder sample. In the inset at the lower right corner, the irregular In_2O_3 NPs without any specific crystal facets yield a straight line with a negative slope without hysteresis, indicating that the magnetic signal from these NPs is covered by the diamagnetic background signal. Hence, the

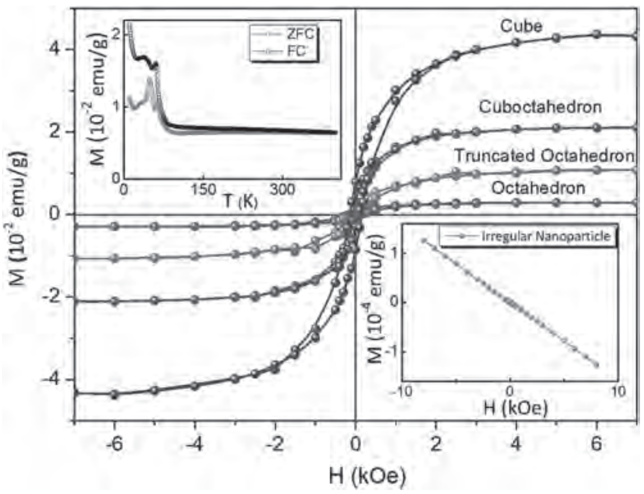

Figure 3. Main panel: *M*–*H* curves of the four In_2O_3 MC samples. The inset at the top left corner shows the ZFC and FC curves at 500 Oe of the cubic In_2O_3 sample and that at the lower right corner shows the *M*–*H* curves of the In_2O_3 NPs with an irregular morphology.

NPs are either nonmagnetic or weakly ferromagnetic with saturated magnetization of no more than 10^{-4} emu g^{-1}. This is consistent with the saturated magnetization of In_2O_3 NPs reported previously.[16,17] The irregular surface cannot provide enough free space for itinerant electrons to move. As a result, the effective density of states for the itinerant electrons is small and cannot support the spin unbalance. Similar to many types of dielectric materials, the response of localized orbitals of electrons to the magnetic field produces diamagnetism in the nonregular NPs.

It has been reported that undoped In_2O_3 NPs with a small size (<12 nm) show weak FM at room temperature because of the increased surface OVs.[16,17] However, our In_2O_3 MCs with a size of about 1 µm show saturated magnetization that is 100 times larger than that of the NPs with a size of a few tens of nanometers. This suggests that the ferromagnetic origin of the undoped In_2O_3 MCs is not simply OVs near the surface. The {001} crystal facets which are not exposed on the NPs with an irregular morphology possibly contribute to the stronger FM of the In_2O_3 MCs by interacting with underlying vacancies.

The temperature dependence of magnetization is measured under a constant magnetic field of 500 Oe and the result is shown in the inset at the top left corner in Figure 3. The divergence between the zero-field-cooled (ZFC) and field-cooled (FC) magnetization curves in the temperature range between 5 and 400 K reveals that the Curie temperature of the cubic In_2O_3 is higher than 400 K[33,34] corresponding to the room temperature FM shown in the *M*–*H* loop. It should be mentioned that although both the ZFC and FC curves show some turning points at low temperature, which is analogous to the curves of spin-glass and superparamagnetic materials, the curves diverge at these turning point indicating that there is more than one magnetic mechanism including antiferromagnetic correlation competing with ferromagnetic order instead of superparamagnetism in the In_2O_3 cubes.[34,35] Even so, the specific {001} crystal facets still play an important role in the enhancement of FM.

To elucidate the ferromagnetic origin, X-ray photoelectron spectroscopy (XPS) is performed to identify OVs in the MC samples. The O 1s spectra of the four samples fitted with two Gaussian functions are presented in **Figure 4**. The lower binding energy peak at 529.7 eV can be assigned to O^{2-} species in the lattice (O_L), whereas the higher energy one at 531.5 eV stems from O^{2-} ions near the OV regions (O_V).[25,36,37] The smaller electron charge density in the OV region reduces the screening effect of the O^{2-} 1s electrons from the nucleus, thereby raising the effective nuclear charge and binding energy of the O^{2-} 1s electron.[32,38] Since the XPS sampling depth is only a few nanometers, the area ratio of the O_V and O_L peaks is related to the concentration of surface OVs labeled in Figure 4. The strongest FM is observed from In_2O_3 cubes with more {001} facets and less OVs and it is consistent with the theoretical investigation discussed above. XPS is also performed on the NPs with an irregular morphology (Figure S6, Supporting Information) and according to the area ratio of O_V to O_L, there are less surface OVs than cuboctahedral In_2O_3 and more surface OVs than cubic In_2O_3. However, they exhibit weaker FM than the four In_2O_3 MC samples or are nonmagnetic. The results indicate the importance of the {001} facets in the production of FM.

Energy-dispersive X-ray spectroscopy (EDS) is performed to determine the chemical composition and In/O atomic ratios in the undoped In_2O_3 MCs. **Figure 5**a–d shows spectra acquired from the In_2O_3 cubes, cuboctahedrons, octahedrons, and irregular NPs, respectively. The sampling depth of EDS is larger than that of XPS and the elements can be measured more accurately. All the peaks in the four spectra

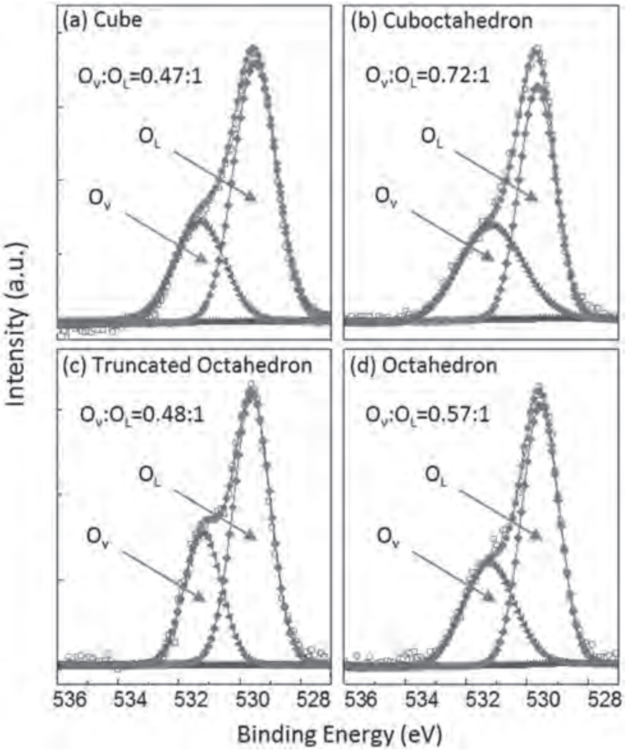

Figure 4. Experimental and fitted curves of the normalized O 1s XPS spectra for the In_2O_3 MC samples: a) cube, b) cuboctahedron, c) truncated octahedron, and d) octahedron.

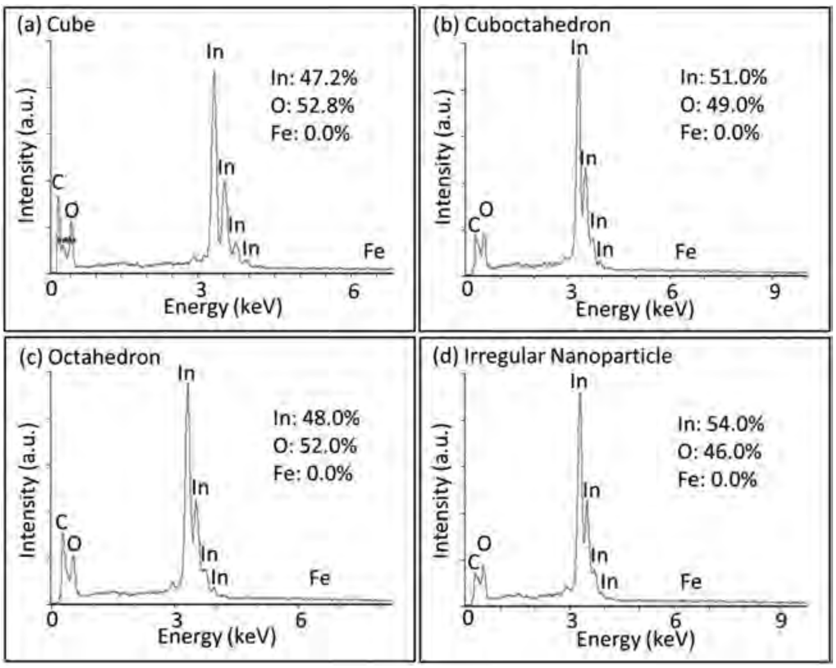

Figure 5. EDS spectra of In_2O_3: a) cube, b) cuboctahedron, c) octahedron, and d) irregular NPs. The elements in the four samples and their atomic percentages are shown in panels. No other magnetic metal impurities such as Fe except indium and oxygen are detected.

can be assigned to indium and oxygen and no Fe or other magnetic elements are detected, providing evidence that the magnetic metal clusters and their oxides do not contribute to the enhanced FM. According to the indium and oxygen atomic percentages at the top right corner, all the In_2O_3 MC samples have surface and bulk OVs or IVs. This bodes well for generation of FM. In particular, the In_2O_3 cubes have a smaller percentage of indium atoms than cuboctahedrons and irregular NPs, thus favoring the formation of IVs on the {001} facets, which is a supplementary factor for stronger FM. In addition, the In_2O_3 cubes enclosed with the {001} facets have almost the same elemental composition proportion as the octahedrons, whereas the cube sample exhibits stronger FM than the octahedron sample. This further verifies the importance of the {001} facets in FM.

Magnetic force microscopy (MFM) images are acquired to disclose the magnetic domains on the high energy {001} and low energy {111} facets. The 3D magnetic amplitude images are depicted in **Figure 6**a and the corresponding topographical height image is presented in Figure 6b. Since the In_2O_3 cubes show an obvious positive magnetic amplitude shift compared to the background signal, all the {001} facets show magnetic domains. The magnetic amplitude image is not exactly the same as the topographical height image due to the heterogeneous magnetic domain distribution on the {001} facets. This suggests that the magnetic signal does not originate from the topography. Figure 6c–f depicts the 2D topographical height, topographical amplitude, magnetic amplitude, and magnetic phase images, respectively, of the two In_2O_3 cubes shown in Figure 6a,b. The two cubes exhibit obvious positive shifts in both the magnetic amplitude and magnetic phase, further indicating the existence of magnetic domains on the {001} facets and FM is quite strong. The topographical height and magnetic phase images of two typical In_2O_3 octahedrons are presented in Figure 6g,h, respectively. The two In_2O_3 octahedrons do not show any magnetic phase shift (same color as the background signal and indistinct octahedral shape stemming from the topography). Therefore, the magnetic domain distribution cannot be detected from the {111} facet enclosing the In_2O_3 octahedral MC. Since oxygen or indium vacancies are always present in these MC samples, the large difference between the FM on the {001} and {111} facets further verifies that the strong FM is related to the exposed specific {001} facets and underlying vacancies, as predicted by our calculation. Hence, FM can be enhanced by controlling the specific crystal facets together with the proper amount of vacancies.

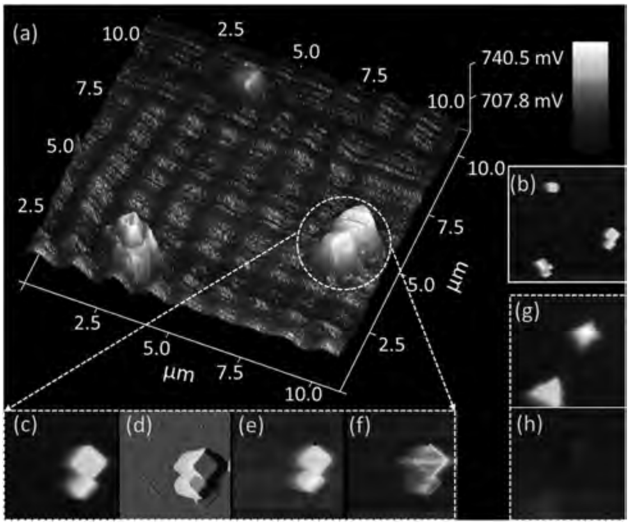

Figure 6. a) 3D magnetic amplitude and b) 2D topography height images of several In_2O_3 cubes. c–f) 2D topography height, topography, and magnetic amplitude, and magnetic phase images of the two cubic In_2O_3. g,h) 2D topography height and magnetic phase images of two In_2O_3 octahedrons as contrast. The bright color indicates the positive shift as shown by the color bar at the top right corner.

3. Conclusion

Ferromagnetism in undoped metal oxide diluted magnetic semiconductors can be enhanced by exposing specific crystal facets via the interaction between surface metal dangling bonds and underlying vacancies. In_2O_3 MCs with a bcc structure are experimentally investigated to corroborate our theoretical prediction and an enhancement of two orders of magnitude is observed from In_2O_3 microcubes with completely exposed {001} facets compared to NPs with an irregular morphology. The concept and methodology described here provide insights in achieving strong room temperature FM in undoped oxide DMSs which have potential in spintronics applications.

4. Experimental Section

Sample Preparation: The In_2O_3 MCs were synthesized under ambient pressure on an improved chemical vapor deposition system. The mixed powders of In_2O_3 (0.35 g) and active carbon (0.15 g) as the precursor were placed on an alumina boat adjacent to a Si substrate. The loaded boat together with a rectangular Si substrate (1 cm × 1 cm) covered by a 10 nm gold thin film was placed downstream in a small quartz tube (inner diameter of 1.6 cm and length of 20 cm) which was positioned in the center of a big horizontal quartz tube (inner diameter of 5.2 cm and length of 120 cm) in a furnace. In the synthesis of In_2O_3 MCs with different morphologies, the furnace was heated to a certain temperature from room temperature in 20 min and remained at that temperature for 3 h under a mixture of Ar and O_2. More details about the sample preparation can be found from the previous paper.[26]

Characterization: The morphology of In_2O_3 MCs was examined by SEM and the microstructure and chemical composition were determined by XRD (Philips, Xpert), XPS (PHI5000 Versa Probe), and EDS. The magnetic tests were conducted on a superconducting quantum interference device (SQUID) and the hysteresis loops of the In_2O_3 MC samples were acquired at 300 K. The temperature-dependent loops were examined at an applied magnetic field of 500 Oe. An atomic force microscope (Digital Instruments, Nanoscope IIIa) was utilized to determine the surface morphology and magnetic domains using the magnetic force microscopic mode. The cantilever oscillating frequency was 60–100 Hz and the module of elasticity was 1–5 N m^{-1}. The tapping mode was adopted to determine the surface morphology and the lift mode was used to obtain the magnetic micrographs with a tip height of 100 nm. In the MFM experiments, the samples were put into deionized water and ultrasonically dispersed. One drop of the suspension after ultrasonic treatment was dripped on the fluorine-doped tin oxide (FTO) film for MFM observation.

Supporting Information

Supporting Information is available from the Wiley Online Library or from the author.

Acknowledgements

This work was supported by the National Basic Research Programs of China under Grants Nos. 2014CB339800 and 2013CB932901 and the National Natural Science Foundation of China (Nos. 11374141, 11404162, and 61521001). Partial support was provided by the City University of Hong Kong Applied Research Grant (ARG) No. 9667122.

[1] J. H. Zhang, S. J. Xiong, X. L. Wu, A. Thurber, M. Jones, M. Gu, Z. D. Pan, D. A. Tenne, C. B. Hanna, Y. W. Du, A. Punnoose, *Phys. Rev. B* **2013**, *88*, 085437.
[2] N. H. Hong, J. Sakai, N. Poirot, V. Brizé, *Phys. Rev. B* **2006**, *73*, 132404.
[3] H. Ohno, *Science* **1998**, *281*, 951.
[4] Z. Q. He, S. J. Xiong, S. Y. Wu, X. B. Zhu, M. Meng, X. L. Wu, *J. Am. Chem. Soc.* **2015**, *137*, 11419.
[5] Z. H. Zhang, X. Wang, J. B. Xu, S. Muller, C. Ronning, Q. Li, *Nat. Nanotechnol.* **2009**, *4*, 523.
[6] J. J. Beltran, C. A. Barrero, A. Punnoose, *Phys. Chem. Chem. Phys.* **2015**, *17*, 15284.
[7] P. Sharma, A. Gupta, K. V. Rao, F. J. Owens, R. Sharma, R. Ahuja, J. M. Guillen, B. Johansson, G. A. Gehring, *Nat. Mater.* **2003**, *2*, 673.
[8] S. Wang, L. Pan, J. J. Song, W. Mi, J. J. Zou, L. Wang, X. Zhang, *J. Am. Chem. Soc.* **2015**, *137*, 2975.
[9] N. Wang, W. Zhou, P. Wu, *J. Mater. Sci.* **2015**, *26*, 4132.
[10] J. Y. Kim, J. H. Park, B. G. Park, H. J. Noh, S. J. Oh, J. S. Yang, D. H. Kim, S. D. Bu, T. W. Noh, H. J. Lin, H. H. Hsieh, C. T. Chen, *Phys. Rev. Lett.* **2003**, *90*, 017401.
[11] D. C. Kundaliya, O. S. B. Kundaliya, S. E. Lofland, S. Dhar, C. J. Metting, S. R. Shinde, Z. Ma, B. Varughese, K. V. Ramanujachary, L. Salamanca-riba, T. Venkatesan, *Nat. Mater.* **2004**, *3*, 709.
[12] M. Venkatesan, C. B. Fitzgerald, J. M. Coey, *Nature* **2004**, *430*, 630.
[13] S. Ning, P. Zhan, Q. Xie, Z. Li, Z. Zhang, *J. Phys. D: Appl. Phys.* **2013**, *46*, 445004.
[14] S. Sun, P. Wu, P. Xing, *Appl. Phys. Lett.* **2012**, *101*, 132417.
[15] A. Gupta, H. Cao, K. Parekh, K. V. Rao, A. R. Raju, U. V. Waghmare, *J. Appl. Phys.* **2007**, *101*, 09N513.
[16] M. Naeem, S. Qaseem, I. Ahmad, M. Maqbool, *J. Nanopart. Res.* **2012**, *14*, 808.
[17] A. Sundaresan, R. Bhargavi, N. Rangarajan, U. Siddesh, C. N. R. Rao, *Phys. Rev. B* **2006**, *74*, 1613036.
[18] A. Sundaresan, C. N. R. Rao, *Nano Today* **2009**, *4*, 96.
[19] X. Wang, Z. Q. He, S. J. Xiong, X. L. Wu, *J. Phys. Chem. C* **2014**, *118*, 2222.
[20] H. Choi, J. D. Song, K. R. Lee, S. Kim, *Inorg. Chem.* **2015**, *54*, 3759.
[21] E. C. Stoner, *Proc. R. Soc. A* **1939**, *165*, 339.
[22] D. Chu, Y. P. Zeng, D. Jiang, Z. Ren, W. Ren, J. Wang, T. Zhang, *J. Mater. Res.* **2011**, *23*, 2597.
[23] S. Yan, W. Qiao, W. Zhong, C. T. Au, Y. Dou, *Appl. Phys. Lett.* **2014**, *104*, 062404.
[24] R. J. Green, D. W. Boukhvalov, E. Z. Kurmaev, L. D. Finkelstein, H. W. Ho, K. B. Ruan, L. Wang, A. Moewes, *Phys. Rev. B* **2012**, *86*, 115212.
[25] L. C. Tien, Y. Y. Hsieh, *Mater. Res. Bull.* **2014**, *60*, 690.
[26] M. Meng, X. L. Wu, X. B. Zhu, L. Yang, Z. X. Gan, X. S. Zhu, L. Z. Liu, P. K. Chu, *J. Phys. Chem. Lett.* **2014**, *5*, 4298.
[27] M. Sun, S. J. Xiong, X. L. Wu, C. Y. He, T. H. Li, P. K. Chu, *Adv. Mater.* **2013**, *25*, 2035.
[28] J. P. Perdew, K. Burke, M. Ernzerhof, *Phys. Rev. Lett.* **1996**, *77*, 3865.
[29] S. J. Clark, M. D. Segall, C. J. Pickard, P. J. Hasnip, M. J. Probert, K. Refson, M. C. Payne, *Z. Kristallogr.* **2005**, *220*, 567.
[30] D. R. Hamann, M. Schluter, C. Chiang, *Phys. Rev. Lett.* **1979**, *43*, 1494.
[31] B. G. Pfrommer, M. Cote, S. G. Louie, M. L. Cohen, *J. Comput. Phys.* **1997**, *131*, 233.
[32] J. B. Goodenough, *Magnetism and the Chemical Bond*, Interscience, New York **1963**.
[33] X. Xu, C. Xu, J. Dai, J. Hu, F. Li, S. Zhang, *J. Phys. Chem. C* **2012**, *116*, 8813.

[34] H. S. S. Ramakrishna Matte, K. S. Subrahmanyam, C. N. R. Rao, *J. Phys. Chem. Lett.* **2009**, *113*, 9982.
[35] J. Zhu, H. Park, R. Podila, A. Wadehra, P. Ayala, L. Oliveira, J. He, A. A. Zakhidov, A. Howard, J. Wilkins, A. M. Rao, *J. Magn. Magn. Mater.* **2016**, *401*, 70.
[36] L. W. Park, H. S. So, H. M. Lee, H. J. Kim, H. K. Kim, H. Lee, *J. Appl. Phys.* **2015**, *117*, 155305.
[37] T. Szörényi, L. D. Laude, I. Bertóti, Z. Kántor, Z. Geretovszky, *J. Appl. Phys.* **1995**, *78*, 6211.
[38] J. C. C. Fan, J. B. Goodenough, *J. Appl. Phys.* **1997**, *48*, 3524.

Received: September 3, 2016
Revised: October 9, 2016